On the dynamics of small-scale vorticity in isotropic turbulence

By J. Jiménez[1] and A. A. Wray[2]

1. Motivation

In a previous report (Jiménez *et al.* 1993, referred from now on as JWSR), it was shown that the strong vorticity in isotropic turbulence is organized into tubular vortices ("worms") whose properties were characterized through the use of full numerical simulations at several Reynolds numbers. That paper should be consulted for details as well as for the previous history of the subject. At the time most of the observations were kinematic, and several scaling laws were discovered for which there was no theoretical explanation. In the meantime, further analysis of the same fields yielded new information on the generation of the vortices, and it was realized that even if they have to had to be formed by stretching, they were at any given moment actually compressed at many points of their axes (Jiménez and Wray, 1994). This apparent contradiction was partially explained by postulating axial inertial waves induced by the nonuniformity of the vortex cores, which helped to "spread" the axial strain and allowed the vortices to remain compact even if not uniformly stretched. The existence of such solutions was recently proved numerically by (Verzicco, Jiménez & Orlandi 1994). The present report discusses a set of new numerical simulations of isotropic turbulence, and a re-analysis of the old ones, in an effort to prove or disprove the presence of these waves in actual turbulent flows and to understand the dynamics, as oposed to the kinematics, of the vortices.

One set of experiments use hyperviscous dissipation instead of regular viscosity. Since the strong vortices are known to be dissipative structures with characteristic radii in the range of the near dissipation range of the turbulence cascade, they can be considered as being forced by inertial range eddies, but to be dominated by viscous diffusion. The hope was that hyperviscosity would change the diffusion mechanism without changing the forcing and give us a better insight into the dynamics. This strategy was largely successful, but some unexpected consequences of hyperviscosity were found in the form of a strong bump in the upper inertial range of the spectrum, spanning at least one and a half decades in wavenumber, and which seems to be an evolution of the much weaker bump described in some experiments in real fluids. This bump is discussed below in detail and may be of some practical relevance since some sub-grid models in LES computations use eddy viscosity laws that resemble hyperviscosity, and the present result suggests that their effect might distort the spectrum across a range of scales comparable to that of most practical LES numerical grids.

1 Also with School of Aeronautics, U. Politécnica, Madrid

2 NASA Ames Research Center, Moffet Field, Ca. 94035

Finally, the study of strong vorticity leads directly to the question of intermittency. It appears that at the Reynolds numbers of our flows ($Re_\lambda \leq 170$), most of the extended tails in the probability density functions of the velocity gradients can be associated to the vortex filaments and scale with Reynolds number in the same way as they do. We show evidence that the volume ratio occupied by the filaments decreases with Re_λ while the intensity of the individual structures increases. This raises the question, already posed in JWSR, of their behavior in the infinite Reynolds number limit. It would appear that the mechanisms described here can not be extended indefinitely as $Re_\lambda \to \infty$ although the limitations of numerical resolution prevent us from giving a definite answer.

The simulations, both viscous and hyperviscous, are described first. The global flow statistics, especially those related to intermittency, are described next, followed by a description of worm properties and a short discussion of the results. The present is an interim report, and more work is needed, especially from the point of view of theoretical analysis.

2. Viscous simulations

The viscous simulations used in this report are essentially the same as in JWSR. The spectral numerical scheme (Rogallo 1981) and other parameters are described in that paper, which should also be consulted for the detailed definitions of the different quantities, which generally follow (Batchelor 1953). Some simulations were continued for a longer time to improve the statistics, and the two lower Reynolds numbers were repeated at higher resolution, $k_{\max}\eta = 4$ instead of $k_{\max}\eta = 2$, to check that the scalings reported in JWSRwere not artifacts of the use of a uniform resolution in Kolmogorov units. No artifacts were found. These new simulations were also used in a separate study of the effect of resolution on both experiments and in simulations (Jiménez 1994b).

Since the time of the previous report, the fields corresponding to the highest Reynolds number ($Re_\lambda = 168$ on a 512^3 grid) became unavailable for further processing. To paliate this problem, a new simulation was run on a 384^3 grid, resulting in $Re_\lambda = 141$. All these simulations, including the older ones, are sumarised in Table 1, which refers only to the numerical resolution $k_{\max}\eta = 2$.

As in the original study, all simulations were forced to reach a statistically stationary state with a given energy dissipation, adjusted to achieve a desired value for $k_{\max}\eta$. In particular, every Fourier velocity coefficient with a wave number such that $k = |\mathbf{k}| \leq 2.5$ was multiplied at each time step by a common real factor, chosen so that the extra energy introduced in that way was equal to the desired energy dissipation.

It was felt that forcing the flow at such low wave numbers could reduce excessively the statistics of the large scales and perhaps affect the flow. To check that effect, two simulations were performed in which the same type of forcing was applied to the spectral shell $3.5 < |\mathbf{k}| \leq 6.5$. In general, few differences were found between the two types of simulations although the new statistics should clearly be better

Re_λ	N	L_ϵ	L_ϵ/λ	L_ϵ/η	$\epsilon L/u'^3$	t/T	$-F_3$
35	64	1.8	2.3	27	1.09	54.2	0.49
63	128	2.2	4.2	65	0.80	9.3	0.50
94	256	2.0	6.3	120	0.72	8.2	0.52
142	384	2.4	9.5	222	0.73	5.9	0.52
168	512	2.4	11.2	286	0.69	5.9	0.52
26	128	0.6	1.7	18	0.96	11.2	0.50
48	256	0.7	3.2	44	0.62	15.1	0.51

TABLE 1. Numerical and flow parameters for the viscous cases analyzed in this paper. t/T is the total run time in eddy turnover units, F_3 is the skewness coefficient, L is the integral scale, and $L_\epsilon = u'^3/\epsilon$ is the eddy dissipation scale. The last two cases were forced at higher wavenumbers as explained in text.

than the older ones. Those differences that were found are discussed below in the corresponding sections, and the flows themselves are documented in Table 1. The better statistics were compensated by the possibility of reaching only much lower Reynolds numbers. Fig. 1 presents compensated spectra for the different flows.

3. Hyperviscosity

Hyperviscosity, the use of the iterated Laplacian in place of the usual dissipative operator, has been used often in the numerical simulation of turbulence in an effort to obtain longer inertial ranges out of a given resolution. The hope has been that its use would not affect the inviscid aspects of the turbulent flow although it clearly changes the characteristics of the dissipative scales. Since the vortices that concern us seem to be dissipative features, hyperviscous simulations were undertaken in the hope of clarifying their dynamics by changing their behavior. Define the hyperviscosity exponent α through the momentum equation,

$$\frac{D\mathbf{u}}{Dt} + \nabla p = (-1)^{\alpha+1}\nu\nabla^{2\alpha}\mathbf{u} \tag{1}$$

The regular Navier-Stokes equations correspond to $\alpha = 1$. In spectral calculations, the dissipative term is obtained by multiplying the Fourier coefficients of the velocity by $|\mathbf{k}|^{2\alpha}$, and there is no reason to restrict α to be an integer although the physical representation of the dissipation operator may be complicated for non-integer exponents.

The first difficulty in analyzing hyperviscous turbulence simulations is to find reasonable scaling quantities. Since the inertial cascade mechanism is not expected to change, the Kolmogorov dimensional arguments should apply, and the inner microscale should depend only on the viscosity coefficient, ν, and of the dissipation,

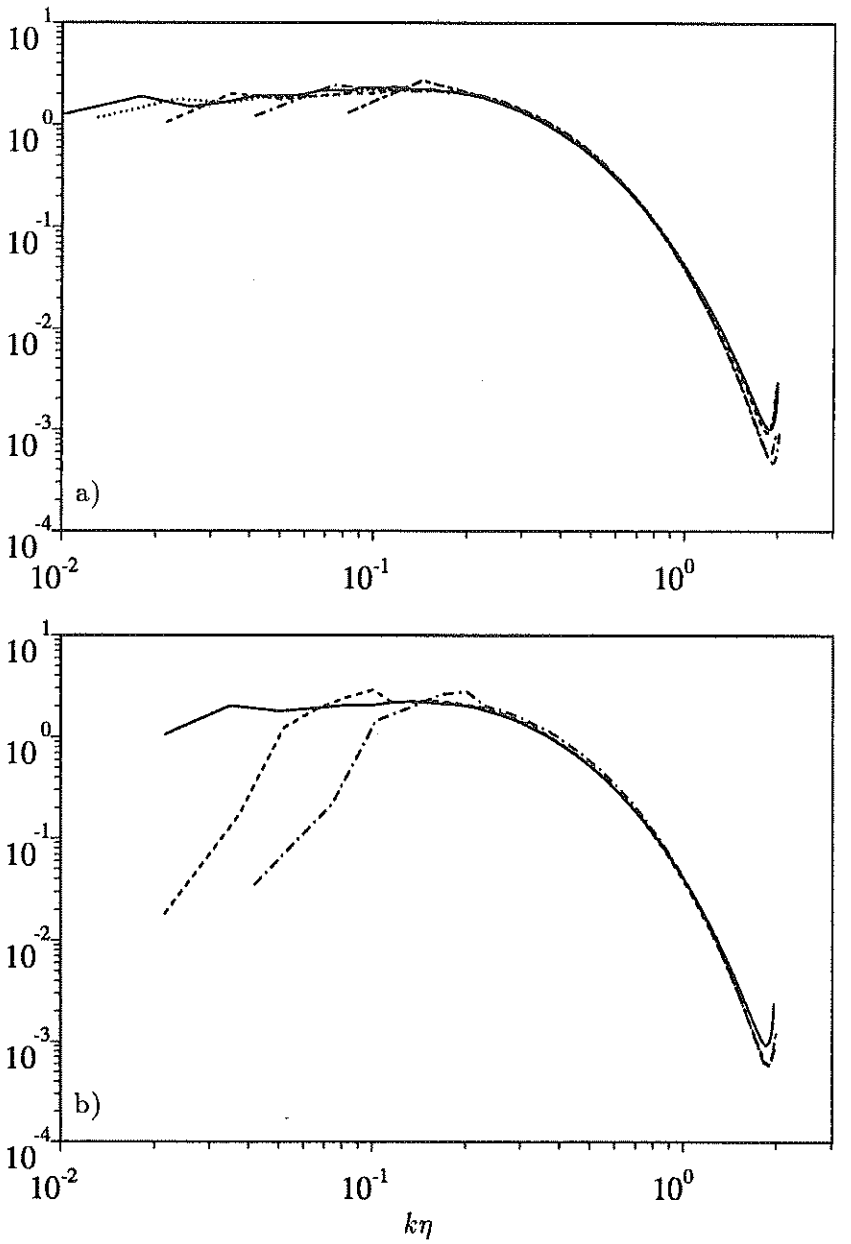

FIGURE 1. Three dimensional compensated energy spectra for the different viscous cases. Vertical axis is $\epsilon^{-2/3}k^{5/3}E(k)$ to enhance the inertial range. a) Forcing at low wavenumbers. ——— : $Re_\lambda = 168$; ····· : 142; - - - - : 94; —·— : 63; — — — : 36. b) Forcing at intermediate wavenumbers. - - - - : $Re_\lambda = 48$; —·— : 26. ——— : $Re_\lambda = 94$ (from Fig. 1a, for comparison).

which is expressed in terms of the energy spectrum as

$$\epsilon = 2\nu \int k^{2\alpha} E(k)\, dk. \tag{2}$$

The inertial scaling is

$$E(k) = v^2 \eta f(k\eta),$$

where

$$v = (\epsilon\eta)^{1/3}, \qquad \eta = (\nu^3/\epsilon)^{1/2(3\alpha-1)}. \tag{3}$$

Note that these definitions agree with the usual ones when $\alpha = 1$, but that ν should not be interpreted as a regular viscosity coefficient, even dimensionally.

There is no unique generalization for the Taylor microscale. In regular turbulence its most obvious use is in defining the microscale Reynolds number Re_λ, which is then related to the ratio of the different length scales as

$$L_\epsilon/\eta = 15^{-3/4} Re_\lambda^{3/2}, \qquad \lambda/\eta = 15^{1/4} Re_\lambda^{1/2}, \tag{4}$$

where $L_\epsilon = u'^3/\epsilon$. If we take these two relations as defining λ and Re_λ, the result is

$$\lambda = \sqrt{15}\,(L_\epsilon \eta^2)^{1/3}, \quad Re_\lambda = 15^{(1-\alpha)/2\alpha} \left(\frac{u' \lambda^{2\alpha-1}}{\nu} \right)^{1/\alpha}, \tag{5}$$

which reduces to the usual one for regular viscosity.

The numerical experiments are listed in Table 2. All except one were conducted at the same numerical resolution, 128^3 and $k_{\max}\eta = 2$, and result in roughly similar Re_λ. A single case was repeated on a larger grid to check Reynolds number scaling. All the fields were forced at $|\mathbf{k}| \leq 2.5$ in the same way as in the viscous cases. One of the quantities listed in the table,

$$\epsilon^* = \epsilon/\nu^{1/\alpha} \omega'^{(3\alpha-1)/\alpha}$$

is a generalization of the equation $\epsilon/\nu\omega'^2 = 1$, which only holds for regular viscosity. The deviation of this coefficient away from unity measures the failure of the vorticity magnitude to represent dissipation in hyperviscous flows.

3.1 Numerics

There are special numerical problems associated with high hyperviscous exponents. The principal one is the limitation imposed to the time increment by the accuracy requirements of the dissipative term. Since most codes implement this substep by some unconditionally stable implicit scheme, the viscous parameter does not represent a stability limitation, but unless the time increment is chosen short enough, the evolution of the velocity due to dissipation will be represented inaccurately, and while the resulting system will usually be equivalent to some dissipative model, it would not be possible to claim that it represents a hyperviscosity of the intended order.

α	Re_λ	N	L_ϵ	L_ϵ/λ	L_ϵ/η	$\epsilon L/u'^3$	ϵ^*	t/T	$-F_3$
1.	63	128	2.2	4.2	65	0.80	1.00	9.3	0.50
1.25	65	128	2.2	4.3	68	0.69	0.57	3.1	0.50
1.50	64	128	2.2	4.2	66	0.68	0.41	3.1	0.49
2.	68	128	2.4	4.5	73	0.66	0.27	3.4	0.49
2.50	68	128	2.5	4.5	74	0.65	0.21	9.5	0.49
4.	75	128	2.8	5.0	86	0.65	0.15	4.8	0.42
2.	95	256	2.0	6.3	121	0.84	0.28	1.5	0.52

TABLE 2. Numerical and flow parameters for the hyperviscous cases analyzed in this paper. The case $\alpha = 1$ is the same one described in Table 1, and is only included here for comparison. The quantity ϵ^* is defined in the text.

Consider a spectral code for the evolution equations (1). The accuracy and stability of the convective term is controlled by the usual CFL parameter, which is proportional to

$$c \sim u' k_{\max} \Delta t, \tag{6}$$

while that of the hyperviscous term is controlled by

$$\delta = \nu k_{\max}^{2\alpha} \Delta t. \tag{7}$$

In our code, which uses an integrating factor for the dissipative term (Rogallo 1981), the modes corresponding to $k_{\max}$ are multiplied every time step by $\exp(-\delta)$, and the explicit integrator for the advection term assumes that this factor is close enough to unity for the accuracy of the nonlinear interactions not to be destroyed during the step. This requires that δ should not be too large. Other implicit schemes have different behaviors, but the accuracy requirement for the dissipative term is always that δ be at most $O(1)$.

The time increment Δt is usually adjusted by fixing the CFL, and the viscous parameter has to be measured. In our code, u' is given by the dissipation ϵ and by the form of the spectrum through the choice of the resolution parameter $k_{\max}\eta$. Assume that $\epsilon \sim u'^3/L \sim u'^3 k_0$, where k_0 is the center of our forcing band. It follows from our definition of the Kolmogorov scale that

$$u' \sim \nu \eta^{1-2\alpha} (k_0 \eta)^{-1/3}. \tag{8}$$

When Δt is obtained using this estimate in the CFL and is then substituted in δ, we obtain

$$\delta/c = \text{const.}\, (k_{\max}\eta)^{2\alpha-2/3} (k_0/k_{\max})^{1/3} \approx 1. \tag{9}$$

From our observations, the empirical constant is approximately 0.03.

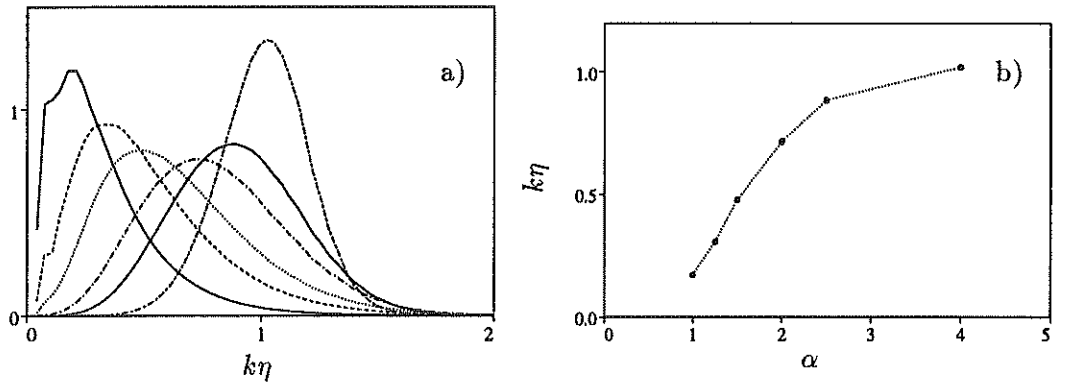

FIGURE 2. a) Dissipation spectra, $\epsilon^{-2/3}\eta^{-5/3}(k\eta)^{2\alpha}E(k)$, for different hyperviscosity exponents. From left to right: $\alpha = 1$, 1.25, 1.5, 2.0, 2.5, 4.0. b) Wavenumber of maximum dissipation.

Fig. 2a displays the hyperviscous dissipation spectra $k^{2\alpha}E(k)$, for various exponents, and Fig. 2b shows the position of the dissipation maximum for the different cases. It is clear from these figures that hyperviscosity succeeds in separating the forcing and dissipation ranges, even at moderate resolutions, although it will be seen below that this does not guarantee an inertial range in the usual sense. It is also clear that $k_{\max}\eta$ should be chosen somewhat larger than unity if the dissipative range is to be reasonably well represented, making the requirement expressed in Eq. (9) more restrictive as the hyperviscosity order increases. In practice, for our choice of $k_{\max}\eta = 2$ and for $k_0 = 2$, $k_{\max} = 60 - 120$ (128^3 or 256^3 grids), it limits our simulations to $\alpha \leq 4 - 5$.

3.2 The near dissipation spectrum

Compensated three-dimensional spectra for some of the hyperviscous fields are presented in Fig. 3a. There is no collapse in the dissipative range, and the qualitative shape of the spectra changes drastically as a function of the hyperviscosity exponent although it should be noted that the two spectra corresponding to the same exponent, $\alpha = 2$, collapse well. As the exponent increases, a large "bump" appears in the near-dissipation range that for the highest exponents and at these low Reynolds numbers, dominates the spectrum. In Fig. 3b, in which the spectrum is premultiplied by k, the bump is seen to behave approximately as k^{-1}.

Anomalous bumps in this region of the spectrum have been reported in experimental viscous flows (Mestayer 1982, She & Jackson 1993, Saddoughi & Veeravalli 1994), and the k^{-1} behavior was claimed by the second of these groups. A theoretical explanation for this power law, based on the depletion of nonlinearity in the near dissipation scales, was offered in (Yakhot & Sakharov 1993). An older explanation for the presence of the bump, although not for the power behavior, is that the outgoing energy cascade is inhibited in the dissipation range since energy has to move into spectral triads with much smaller amplitudes than those corresponding to the equilibrium $k^{-5/3}$ spectrum while the incoming energy is not subject to that

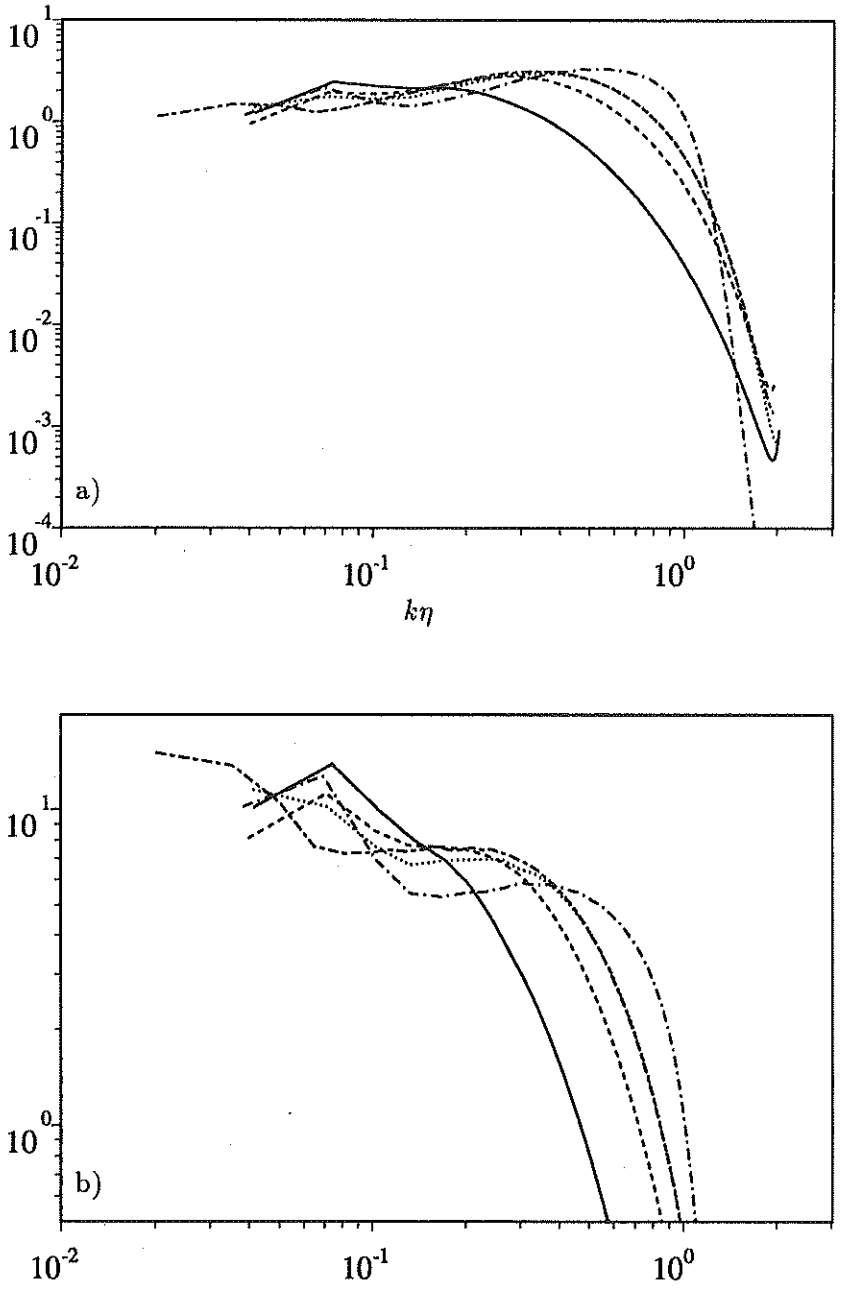

FIGURE 3. Three-dimensional energy spectra for different hyperviscosity exponents. a) $\epsilon^{-2/3}k^{5/3}E(k)$, to enhance inertial range. b) $(\epsilon\eta)^{-2/3}kE(k)$, to enhance the near dissipation bump. ——— : $\alpha = 1$; - - - - : 1.5; ····· : 2.0; —·— : 4.0. All at 128^3 resolution. —— curve: $\alpha = 2.0$, 256^3. This curve overlaps the dotted one in the dissipation range.

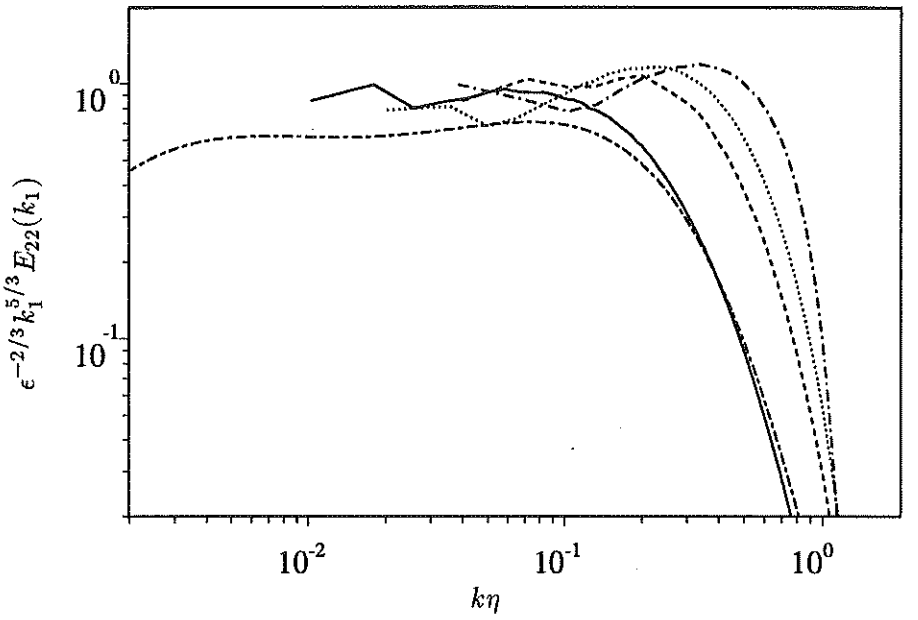

FIGURE 4. Compensated transverse spectra showing extent of near dissipation bump. ——— : $Re_\lambda = 168$, $\alpha = 1$; dashed: $Re_\lambda = 64$, $\alpha = 1.5$; ····· : $Re_\lambda = 96$, $\alpha = 2$; —·— : $Re_\lambda = 64$, $\alpha = 4$; —··— : $Re_\lambda = 600$, $\alpha = 1$, after (Saddoughi & Veeravalli 1994). The peak in the lowest wave numbers of all the numerical spectra is spurious due to forcing scheme.

inhibition. The bump is a consequence of the resulting enery "bottleneck" in the cross-over region (Falkovich 1994). The latter author has described the same spectral behavior in wave turbulence (Ryzhenkova & Falkovich 1990) and has remarked that it would become more pronounced in hyperviscous simulations as the damping becomes more abrupt. The effect is present in spectral turbulence models and has been observed in EDQNM based simulations (Mestayer, Chollet & Lesieur 1983). Finally, some recent hyperviscous simulations of isotropic turbulence, using $\alpha = 8$, have also reported the presence of a k^{-1} bump (Borue & Orszag 1994).

Since it is known that the near dissipation region contains strong vortex filaments, they may also provide an explanation for the k^{-1} behavior. That randomly oriented vortex filaments would generate a spectrum with this behavior was first noted by Townsend (1951) and observed directly in JWSR by computing the spectrum of a flow in which all the vorticity, except the one contained in the strong filaments, had been zeroed. Moreover, an (inviscid) infinite vortex filament is an equilibrium solution of the Euler equation for which, by definition, all the nonlinear interactions cancel identically, and for which the turbulent cascade is fully absent, even if the filament itself is usually formed by the cascade mechanism of vortex stretching. In this sense the three explanations are not necessarily incompatible, and the filament hypothesis merely points to a possible physical implementation of the two previous

ideas.

However, it will be shown below that in the course of the present investigation, we were not able to find significant differences between the structure or frequency of filaments in viscous and hyperviscous flows, which may explain the presence of stronger bumps in the latter. As a consequence the filament explanation remains unlikely. Also, our observations cast doubts on the -1 exponent as a preferred spectral law.

In Fig. 4 we present transverse compensated spectra from several simulations, including our highest Reynolds number regular viscosity case, together with a experimental spectrum from (Saddoughi & Veeravalli 1994). The bump is clearly seen in the experimental spectrum and, in retrospect, also in the regular viscous simulation, showing that even the highest Reynolds number computed by us is far from containing a true inertial range.

Figs. 5a-b display the local logarithmic slope, $d(\log E)/d(\log k)$, for the different spectra in the near dissipation region. They also include data from (Saddoughi & Veeravalli 1994) although in this case, to make it comparable to ours, it is in the form of a three-dimensional spectrum obtained from their data for E_{11}, using the assumption of isotropy. Fig. 5a, for the regular viscous cases, reinforces the conclusion that all our simulations are far from the real inertial range. Fig. 5b, which contains the hyperviscous cases, shows a steady climb of the least negative slope with increasing α with no sign of saturating at k^{-1}. Moreover, the two Reynolds numbers at $\alpha = 2$ show the same tendency as the regular viscous cases with the spectral hump extending further into the low wavenumber range, suggesting that these simulations are also far from reaching a true inertial range and that the extent of the bottleneck region is not shortened by the sharpening of the dissipation peak.

4. Velocity gradients

It has been known for a long time that the probability density functions for velocity differences become increasingly non-Gaussian at short distances, and that this leads to highly intermittent behavior of the velocity gradients, which becomes more pronounced at high Reynolds numbers. In JWSRwe presented histograms for different combinations of gradients (vorticity and total strain magnitudes and local stretching, $\sigma = \omega S \omega / \omega^2$), which clearly showed this Reynolds number effect. A compact representation of this departure from Gaussianity is provided by the high order flatness and skewness $F_n(\zeta) = < \zeta^n > / < \zeta^2 >^{n/2}$, two of which are given in Fig. 6 for the viscous and hyperviscous cases. In each case the vertical origin of coordinates has been chosen to coincide with the Gaussian value ($F_4 = 3$, $F_6 = 15$. The tendency for both flatnesses to grow with Reynolds number is clear, as is the fact that the simulations forced at intermediate wave numbers do not differ significantly in this respect from those forced at low wave numbers. The values for the fourth order flatness of the longitudinal gradients agrees well with the compilation in (Van Atta & Antonia 1980) although our experiments cover a much narrower range of Reynolds numbers than theirs.

The variation of the flatness with the hyperviscosity exponent (Fig. 6b) is more

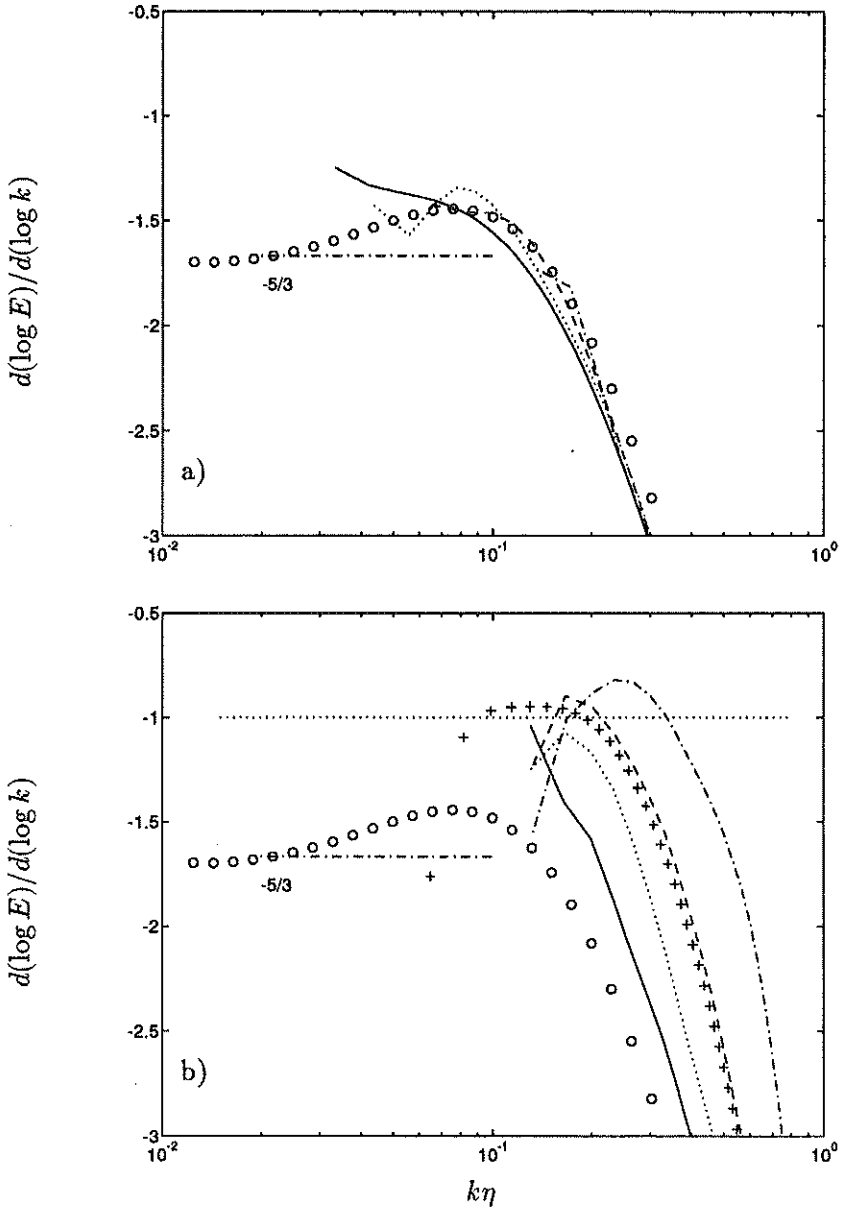

FIGURE 5. Logarithmic slope for the different three-dimensional energy spectra, in the near dissipation region. a) Regular viscosity. ——— : $Re_\lambda = 168$; ····· : 141; - - - - : 98; —·— : 65. b) Hyperviscosity. ——— : $\alpha = 1.25$; ····· : 1.5; - - - - : 2. ($Re_\lambda = 68$); +: 2. ($Re_\lambda = 94$); —·— : $\alpha = 4$. In both figures, open circles are experimental data from (Saddoughi & Veeravalli 1994) at $Re_\lambda = 600$.

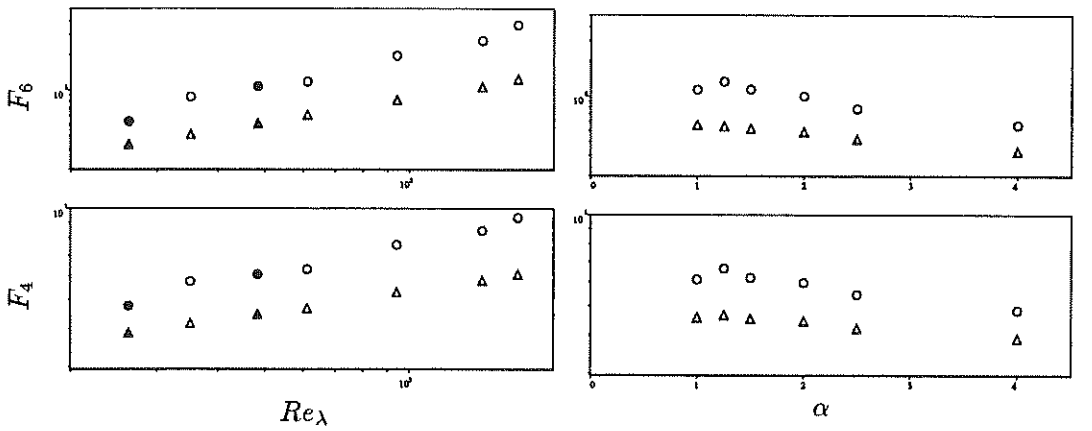

FIGURE 6. Fourth and sixth order flatness factors for velocity gradients. (a) Viscous simulations vs. Reynolds number. (b) Hyperviscous simulations vs. exponent; $Re_\lambda \approx 65$. $\triangle$: longitudinal gradients, $\partial u/\partial x$. $\circ$: transverse, $\partial u/\partial y$. Open symbols are flows forced at low wave numbers. Closed symbols are forced at intermediate wave numbers.

surprising. While it seems from table 2 that the equivalent Reynolds number increases slightly with increasing α and while the same conclusion could be reached from the increasing separation between the integral scales and the dissipation peak (Fig. 2a), the flatness is seen to decrease with α. The same behavior is observed in the histograms of almost all the gradient quantities, as can be seen for the vorticity magnitude in Fig. 7a. The exception is the stretching histogram (Fig. 7b) which shows a much weaker variation with α, essentially within the statistical uncertainty.

It should be stressed that the variation of the flatness with Re_λ is similar in the hyperviscous flows at constant α and in the viscous ones. This is clear from table 3, which contains flatness for the two Re_λ available at $\alpha = 2$. There is also a consistent, although much weaker, increase in the skewness, F_3, with Re_λ which can be seen from tables 1 and 2, and which is also in general agreement with the data in (Van Atta & Antonia 1980).

5. Worms

An algorithm was developed in JWSR to track individual filaments and to measure their properties. The same algorithm has been used here to analyze the new flow fields and to obtain data which may be useful in understanding their dynamics. The axis of each filament is followed until some arbitrary definition of its end point is reached and the vortex radius, circulation, peak axial vorticity, and axial stretching are measured at each point and used to compile statistics over the fraction of the flow contained in the worms.

The axial stretching is defined as $n_i S_{ij} n_j$, where S_{ij} is the strain tensor and n_i is the unit vector in the direction of the axis. The condition to end a filament was

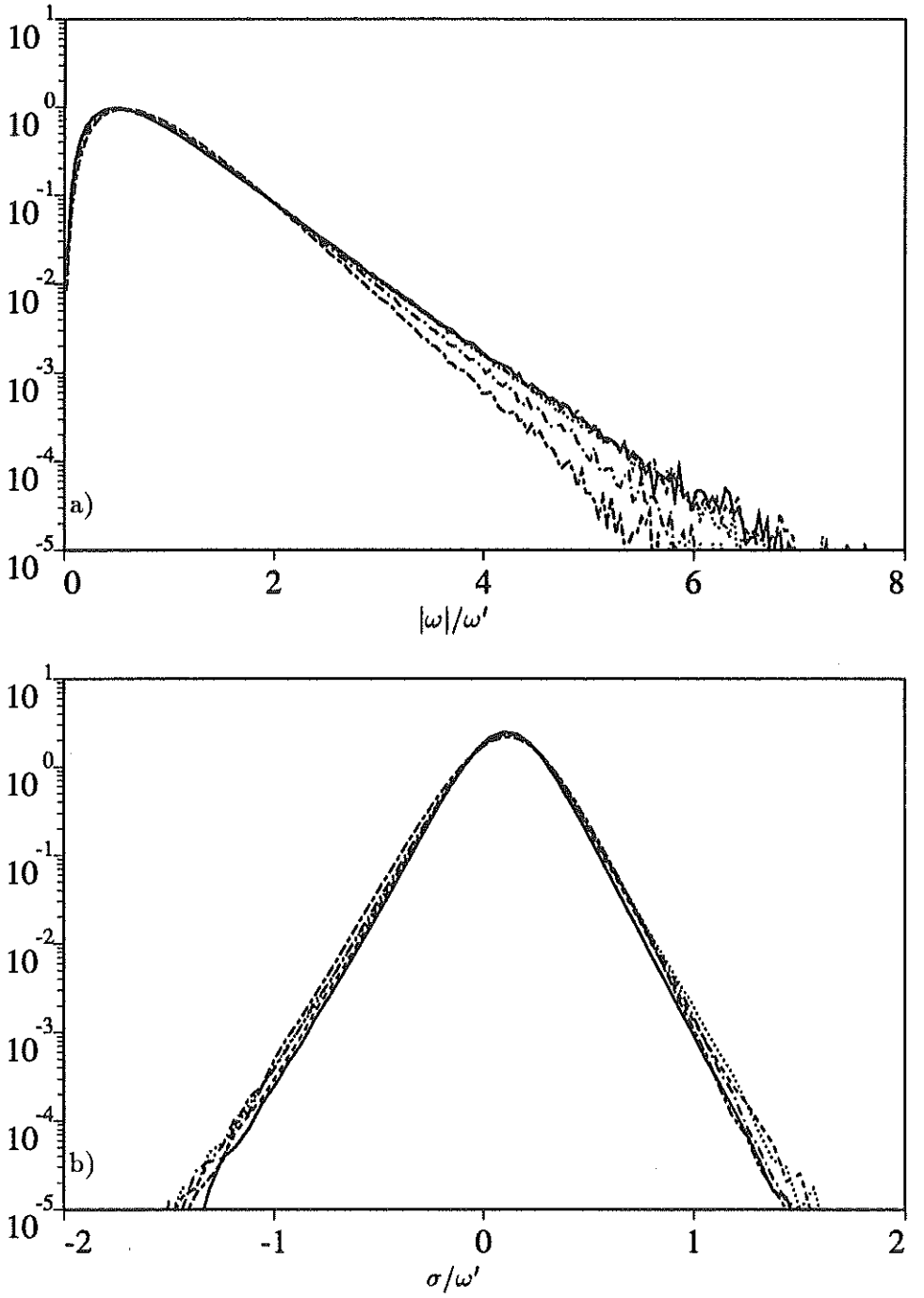

FIGURE 7. Probability density functions of (a) Vorticity. (b) Stretching rate. In all cases $Re_\lambda \approx 65$. ——— : $\alpha = 1$; - - - - : 1.5; ····· : 2; —·— : 2.5; — — — : 4.

Re_λ	$F_{4\ell}$	F_{4t}	$F_{6\ell}$	F_{6t}
68	4.5	5.9	49	100
95	4.8	6.5	62	131

TABLE 3. Flatness factor for the two hyperviscous cases with $\alpha = 2$. Subscript ℓ refers to longitudinal gradients, t to transverse ones.

described in detail in JWSR but depends essentially on the axial vorticity weakening below a given level.

The simplest statistic is the mean value of a given property over all the axial points of all the worms detected in a given flow. There are two groups of properties. Since filaments have to be formed by stretching of preexisting vorticity, the axial stretching can be considered as the driving force in the formation of the worms while all the other properties can be considered as the results of that forcing.

Both groups behave differently. The mean value of axial stretching, averaged over the axes of the worms, is shown in Fig. 8 normalized with the rms value of the vorticity over the whole flow, which is the natural scaling for the velocity gradients in the bulk of the flow. Except for a slight tendency to grow with Re_λ, the stretching scales well with ω' although the proportionality constant depends on the hyperviscosity exponent. It was shown in JWSR that the average stretching, conditioned on a given vorticity, depends only weakly on the conditioning value, and this was interpreted as an indication that the filament did not stretch itself appreciably. The present result reinforced that conclusion since it will be seen below that the mean vorticity in the worms is a fairly strong function of Re_λ while we have shown that the stretching is not.

This is further confirmed by Figs. 9 and 10, which show correlation functions and lengths for the axial distribution of the stretching along worms. The correlation length is a useful indication of the typical length scale of a given property, and we use it here as a less subjective indication of length than the one used in JWSR, which was based on the total length of the detected worms.

Consider a quantity, $\zeta(s)$, given as a function of arc length along the axis and assumed to have zero mean value, and define the correlation

$$R(s) = < \zeta(s')\zeta(s'+s) > / < \zeta^2 >, \tag{10}$$

where the average is taken over the axial position s'. This function has zero integral and $R(0) = 1$. It will first become negative at some point $s = s_0$ (Fig. 9). We define the correlation length as

$$\ell_\zeta = \int_0^{s_0} sR(s)\,ds / \int_0^{s_0} R(s)\,ds. \tag{11}$$

The same definition can be used on properties which are defined at all points in the flow for which the arc length s has to be substituted by a coordinate distance

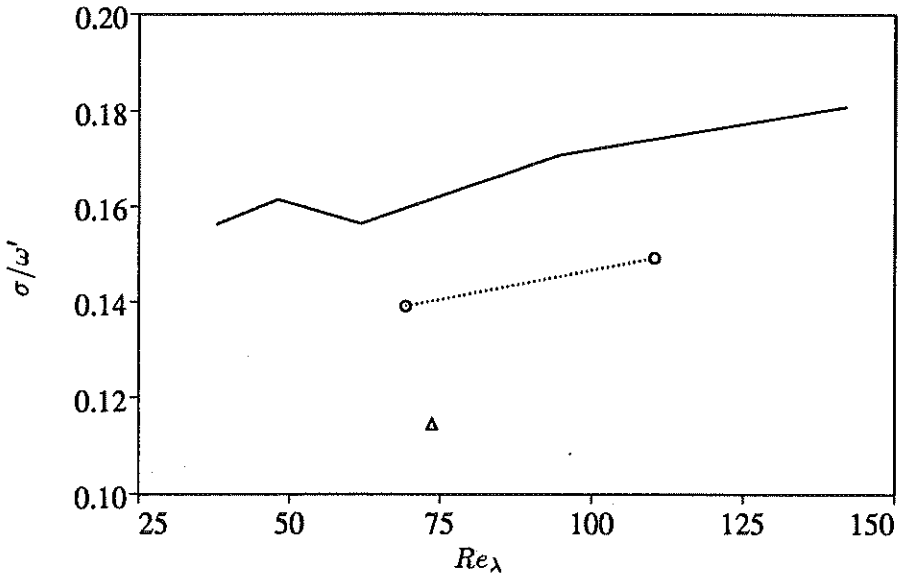

FIGURE 8. Average axial stretching along filament axes. ——— : viscous flows; o : $\alpha = 2$; △ : $\alpha = 4$.

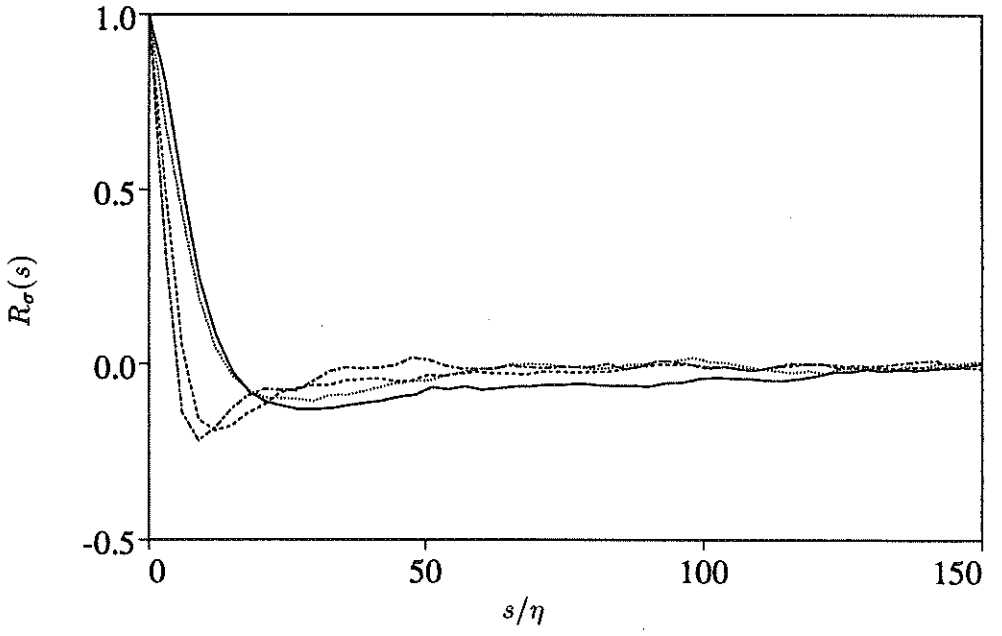

FIGURE 9. Correlation functions of axial stretching, against of the arc length along the worm axes. ——— : $\alpha = 1$, $Re_\lambda = 63$; ····· : $Re_\lambda = 142$; - - - - : $\alpha = 2$, $Re_\lambda = 68$; —·— : $\alpha = 4$.

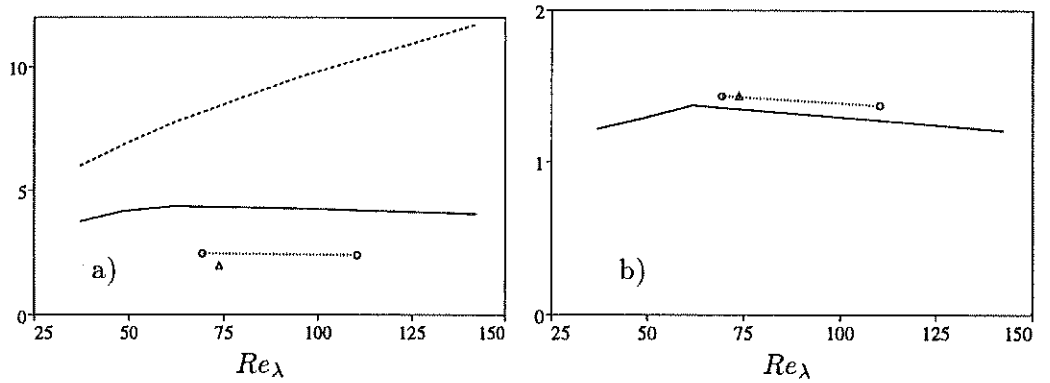

FIGURE 10. Axial correlation length of the stretching along the filament axes. (a) Normalized with the Kolmogorov length. (b) Normalized with the correlation length of longitudinal gradients over the whole flow. Symbols as in Fig. 8. The dashed line in (a) is the Taylor microscale, for comparison.

(e.g. x). This global correlation function can be computed as the inverse Fourier transform of the one-dimensional spectrum of the quantity (Batchelor 1953). From that, and since the power spectrum of the velocity gradients has its maximum at the near disipation region, it follows that the correlation lengths for gradients when averaged over the whole flow should scale with η.

Fig. 10a shows the correlation length for the stretching along the worms, ℓ_σ, which scales well with η, although the scaling constant depends again on the hyperviscosity exponent. This is not surprising since we have shown that the shape of the near dissipation spectra depends on α and so does presumably the relation between the size of the gradient eddies and η. In Fig. 10b we show ℓ_σ normalized with the correlation length of the longitudinal gradients $\partial u/\partial x$ taken over the whole flow. Most of the dependence with α disappears, and the ratio is close to one, showing once again that the stretching along the worms is essentially indistinguishable from that at a generic point in the flow and that self stretching is not important.

It is therefore surprising that the axial correlation lengths of all the resulting worm properties are much larger than η and scale apparently on the integral scale of the flow (Fig. 11). This generalizes the observation in JWSR, which has been made by all the investigators that have studied these filaments, that their length is of the order of the integral scale. While the original observations were made on the basis of arbitrary visualization or termination criteria, the present result is a more objective characterization of the same phenomenon. In these last two figures we have included a curve for the Taylor microscale λ which is defined by Eq. (4). This is done mainly for comparison, but also because this scale has been suggested often as a natural scale for the turbulent eddies. In particular, it was observed in JWSR that if the characteristic stretching along worms was of $O(\omega')$ and since it is known that the velocity differences in a turbulent flow scale with u' without strong Reynolds number effects, the largest possible length scale for the stretching was $O(\omega'/u') = O(\lambda)$. It was felt at the time that this contradicted the observation

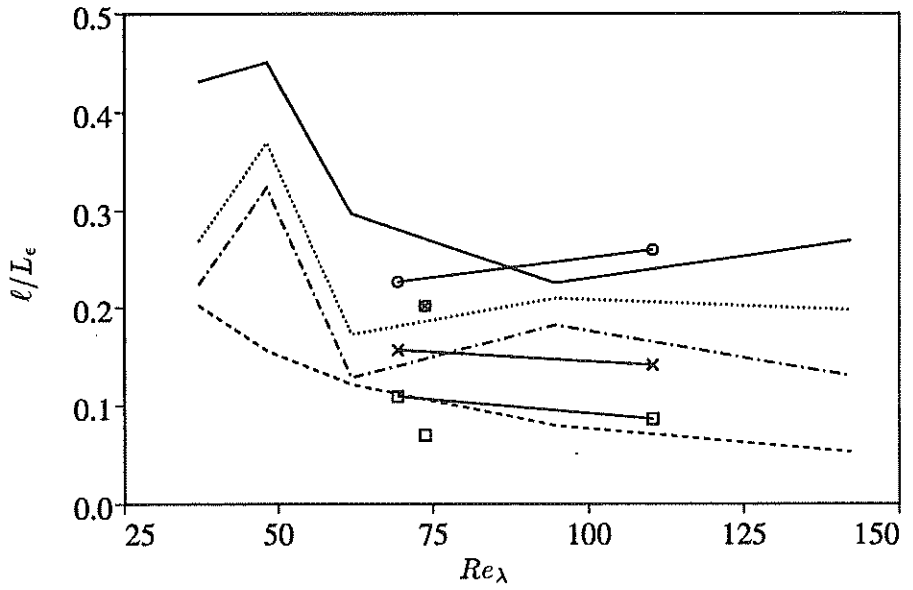

FIGURE 11. Axial correlation lengths along worms axes, normalized of the dissipation length L_ϵ. ——— and o : axial vorticity at axis; ····· and ×: circulation; —·— and □ : radius. Lines without symbols are viscous simulations. Lines with symbols are are $\alpha = 2$. Isolated symbols are $\alpha = 4$.

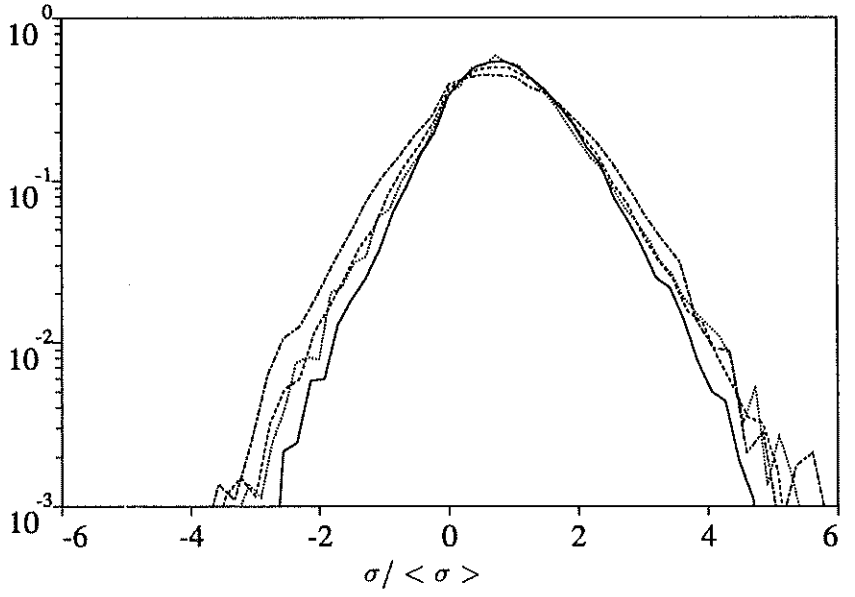

FIGURE 12. Probability density function for the stretching σ along the axes of the worms. Symbols as in Fig. 9. All histograms are normalized to unit mean value.

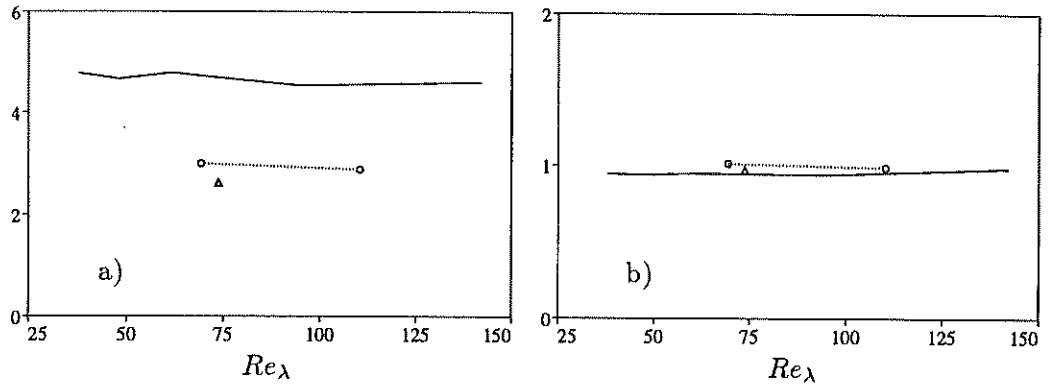

FIGURE 13. Mean worm radius. (a) Normalized with the Kolmogorov length. (b) Normalized with Burgers' radius for the average axial strain. Symbols as in Fig. 8.

that the length of the worms was $O(L_\epsilon)$ since it was assumed that vortices could only survive if stretched on the average. This proved to be false, and it was shown in (Jiménez & Wray 1994) that the strain along the worms is compressive over a large fraction of the axis (Fig. 12). Verzicco, Jiménez and Orlandi (1994) have shown recently by direct computation that vortices subject to spatially nonuniform axial strain, even one with zero axial average stretching, can reach a steady state thanks to the presence of axial inertial waves which "smooth" the strain over the compressive parts.

It is still interesting to note that although the L_ϵ scaling seems to be a better representation of the data in Fig. 11, especially at the higher Re_λ, a scaling of a few Taylor microscales is not completely incompatible with them.

In (Jiménez & Wray 1994) the equivalent to Fig. 12 was plotted together with probability density functions of the same quantity computed over the whole flow field. The differences between the two were shown to be small, stressing again that the forcing of the filaments is not different from that of the rest of the flow. Note however that the collapse of the stretching pdf's over the full field for different values of α (Fig. 7b) is better than those of the same quantity over the worms (Fig. 12), suggesting either that there is a selection mechanism for the location of worms in terms of stretching or a dynamical feedback from the worms into the structure of the stretching itself. The same conclusion can be drawn from the dependence of the average worm stretching on α, shown in Fig. 10.

The average radius of the worms is given in Fig. 13a. It scales with the Kolmogorov scale although there is again a different proportionality constant for different hyperviscosity exponents. A better collapse is possible if we assume that the filaments are Burgers' vortices driven by the mean axial strain. For viscous flows, the Burgers' radius due to a strain ω' is $2(\nu/\omega')^{1/2} = 2\eta$, which agrees with the approximate Kolmogorov scaling for these flows in Fig. 13a.

Hyperviscous Burgers' vortices were computed in (Jiménez 1994a). Although their outer tails are different from the viscous ones and actually change sign before

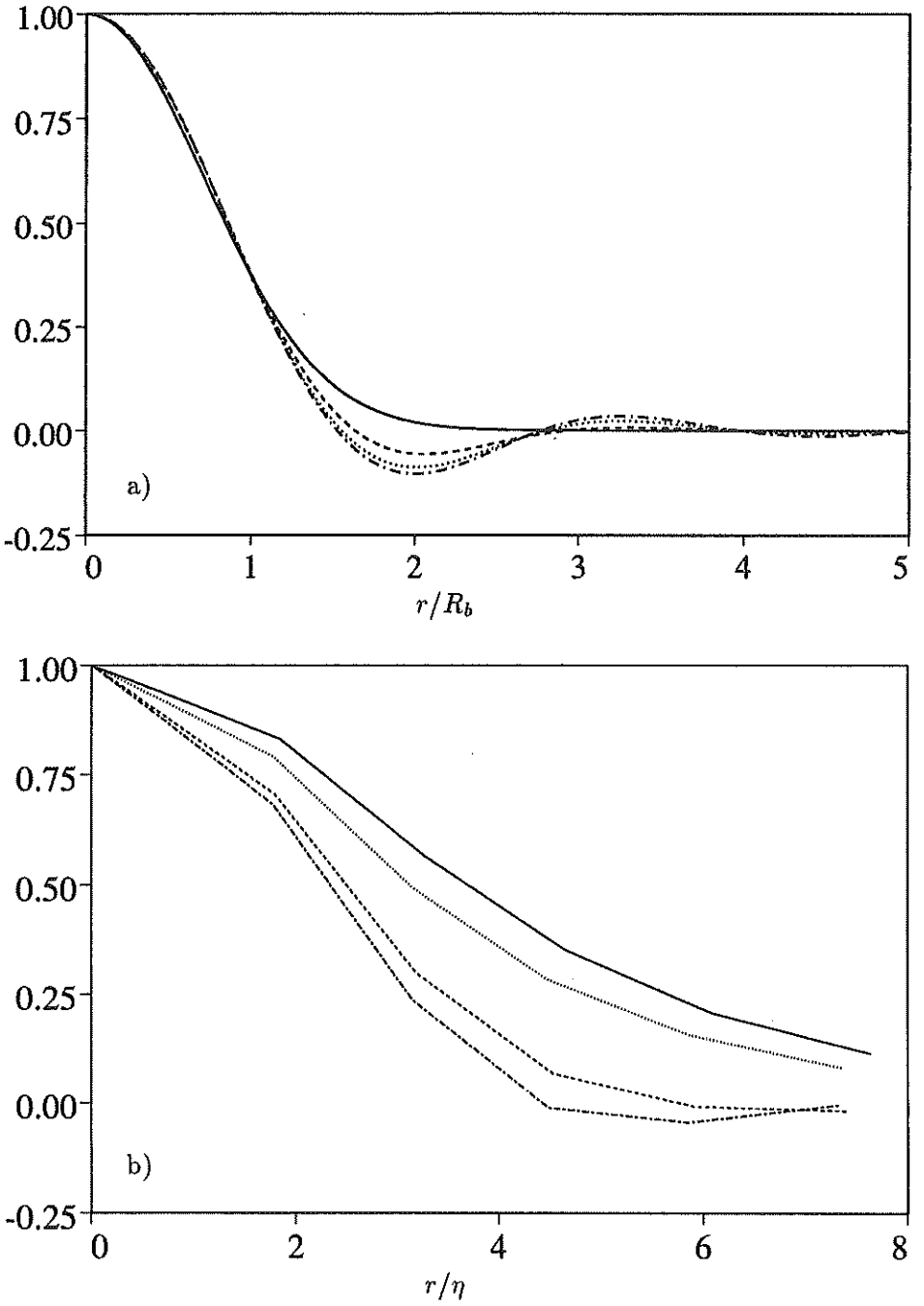

FIGURE 14. (a) Radial vorticity distribution for hyperviscous Burgers' vortices, normalized using Eq. (12). ——— : $\alpha = 1$; - - - - : 2; ····· : 3; —·— : 4. (adapted from Jiménez 1994a). (b) Mean radial distribution of axial vorticity in worms. Symbols as in Fig. 9.

they settle to zero, their cores are approximately Gaussian (Fig. 14a) with a $1/e$ radius which can be approximated for $\alpha \leq 5$ by

$$R_b = (2.022 - 0.0843\alpha + 0.0688\alpha^2 - 0.0086\alpha^3)(\nu/\sigma)^{1/2\alpha}, \tag{12}$$

where the coefficient is the result of a polynomial fit to the solution of an ordinary differential equation. When this formula is used to compute the Burgers' radius associated to the measured mean stretching from Fig. 8, the results are the normalized radii in Fig. 13b, in which the effect of hyperviscosity is essentially absent.

Fig. 14.b contains vorticity profiles averaged along the axes of all the worms in a given flow. The profiles are also approximately Gaussian, and it is interesting to note that the more hyperviscous profiles show signs of negative vorticity at the edges, which may be a reflection of the oscillations in the tails of the theoretical solutions.

Full probability density functions for the local radius and for the radius divided by the *local* Burgers' radius are given in Fig. 15. To avoid effects related to the variations of the mean values, the averages of all those distributions are adjusted to unity. The collapse of the Burgers' plot is excellent, but there is some differences between the pdf's of the raw radii in viscous and in hyperviscous flows, probably reflecting the differences in the structure of the local stretching that were discussed above.

The mean values of the vorticity at the axes of the worms are given in Fig. 16a. It was suggested in JWSR that ω/ω' increases with Reynolds number as $Re_\lambda^{1/2}$ and that same normalization is used in the figure. Except for the case at $Re_\lambda = 48$ in which the forcing was done at higher wave numbers, it seems to work correctly. The intermediate forcing seems to work differently from all the other flows for all quantities which scale with the integral length as can also be observed in Fig. 11. The large scales are different from those of the flows forced at lower wave numbers, and it appears that the axial distribution of vorticity in the worms is controlled by them. A line corresponding to $\omega \sim \omega'$ is also included in the figure and is incompatible with the data. In Fig. 16b we have represented the mean value of the vortex circulation, normalized with the mean vorticity and radius for each flow. It clusters around unity in what is essentially a consistency check for the averages, but which also reflects that the statistical distribution of vorticity and radius are relatively independent of the dissipation model. A few representative pdf's are given in Fig. 17, normalized to unit mean. The sharp cut-off of the vorticity pdf is artificial. The tracking algorithm terminates a worm whenever its axial vorticity falls below ω'.

It is finally interesting to enquire which is the relative importance of worms with respect to the bulk of the flow. This is largely a matter of definition, but a volume fraction can be defined by taking the mean vorticity detected at the axes by our algorithm and defining as worms all the points whose vorticity magnitude is above that threshold. This, although arbitrary, seems justified since it appears from Fig. 17a that our threshold is below the maximum of the distribution and is probably not distorting the mean value too much. When this is done, a volume fraction can

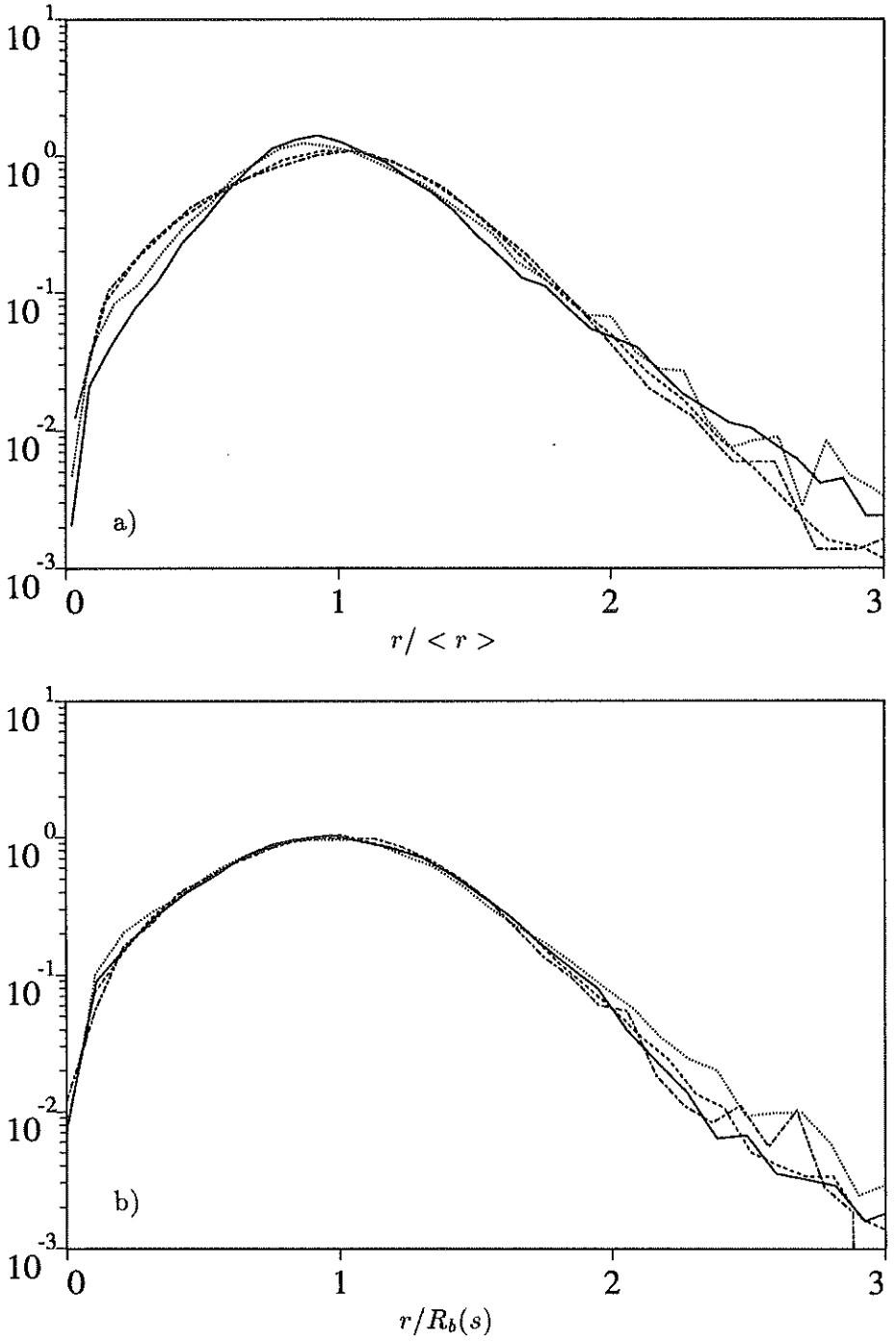

FIGURE 15. Probability density functions for the radius of worms, adjusted in each case to unit average. (a) Radius. (b) Radius divided by local Burgers' radius. Symbols as in Fig. 9.

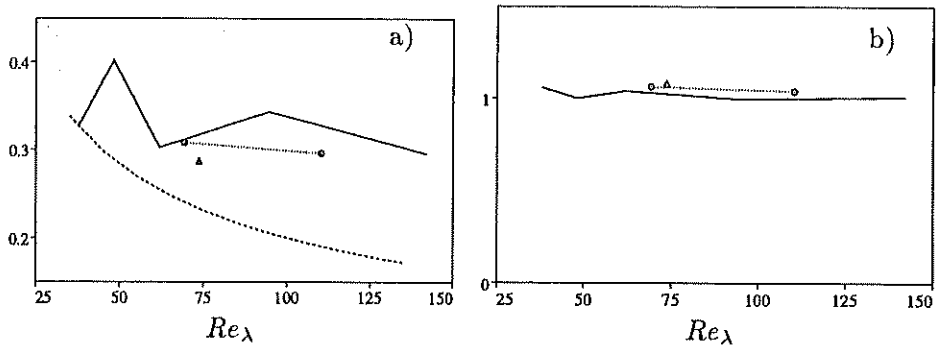

FIGURE 16. (a) Mean vorticity along worm axes, normalized with $\omega' Re_\lambda^{1/2}$. Symbols as in Fig. 8. Dashed line corresponds to $\omega \sim \omega'$, without Reynolds number dependence. (b) Mean value of filament circulation, normalized with mean vorticity and vortex radius, $< \gamma > /\pi < \omega >< r >^2$.

be read from the vorticity histogram of the flow (Fig. 7a) and is represented in Fig. 18. The volume occupied by the worms decreases with Reynolds number as Re_λ^{-2}. Since their characteristic vorticity increases only with $Re_\lambda^{1/2}$, this implies that not only the volume, but also the enstrophy contained in them decreases rapidly as the Reynolds number increases.

6. Conclusions and future work

We have shown that the vortex strong filaments in isotropic turbulence have lengths and axial correlation lengths of the order of the integral scale of the flow, even if the stretching along their axes has a spatial scale of the order of the Kolmogorov length and seems essentially indistinguishable from the strain in the bulk of the flow. We have also shown that the average radius of the vortices is very close to the Burgers' radius corresponding to the mean axial strain, even if large segments of the axes are actually under compression. We have suggested that this is accomplished through the action of axial waves, which distribute the effective strain along the axes. All these observations hold for hyperviscous flows with the obvious modifications needed to accommodate the different core structure of the vortices.

We can think of few mechanisms to generate coherent vortices of such lengths in turbulent flows. The obvious one, in which vortices form by roll-up of the large scale vorticity layers in between large eddies, is unlikely because it can readily be shown that the large-scale stretching is at most able to collapse vortices to radii of the order of the Taylor microscale, and it is difficult to think of a way in which straining motions of the observed scales, η, could further collapse these cores, much thicker than themselves, into more compact cores.

Another possibility, and the one that we favor at the moment, is a mechanism by which short vortex "sticks" form individually and are later patched by the axial waves into longer units. This mechanism has been demonstrated in simpler situations in (Verzicco, Jiménez and Orlandi 1994). Note that from Figs. 10 and 11, the

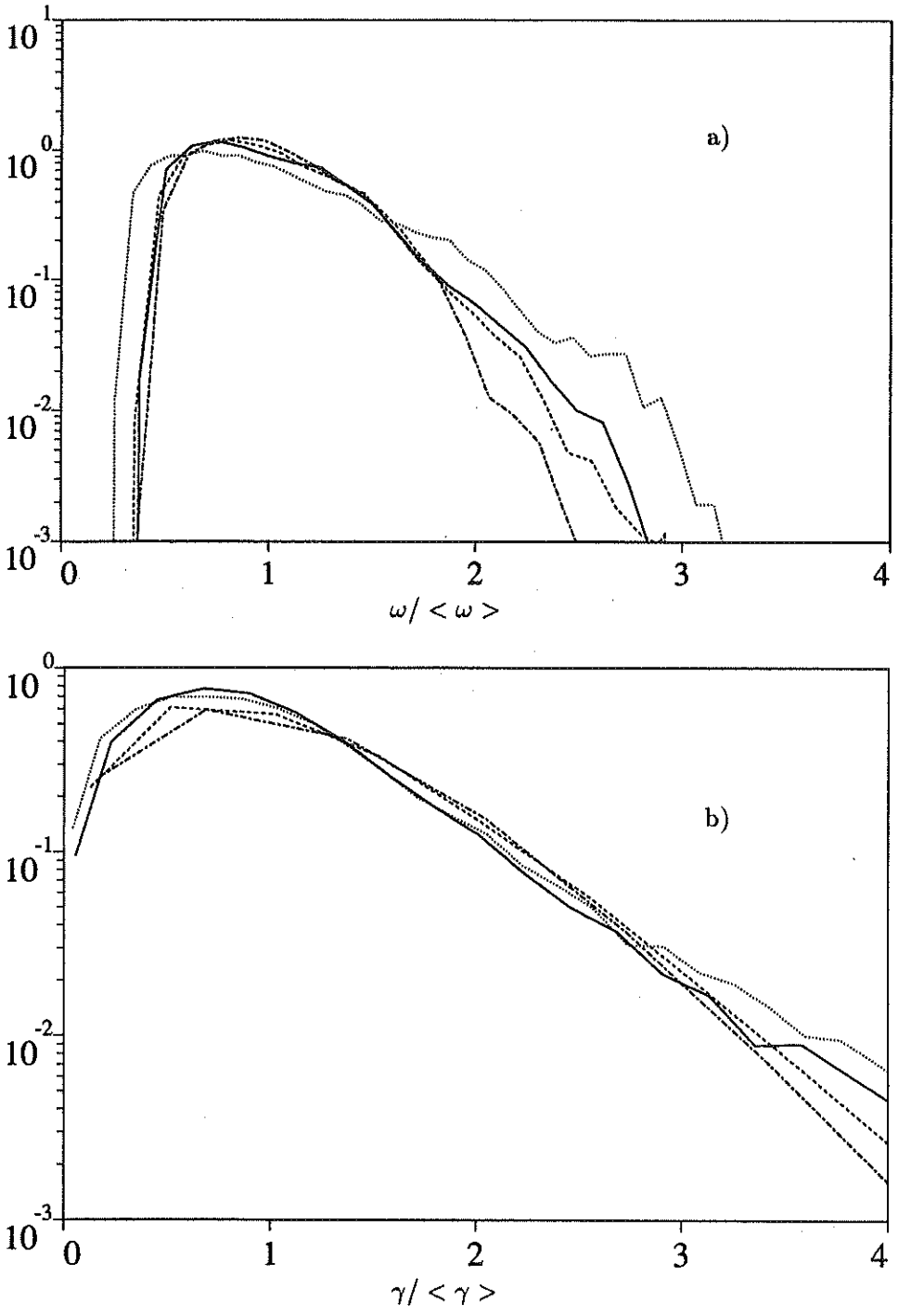

FIGURE 17. Probability density functions for (a) vorticity at worm axis. (b) Circulation, adjusted in each case to unit average. Symbols as in Fig. 9.

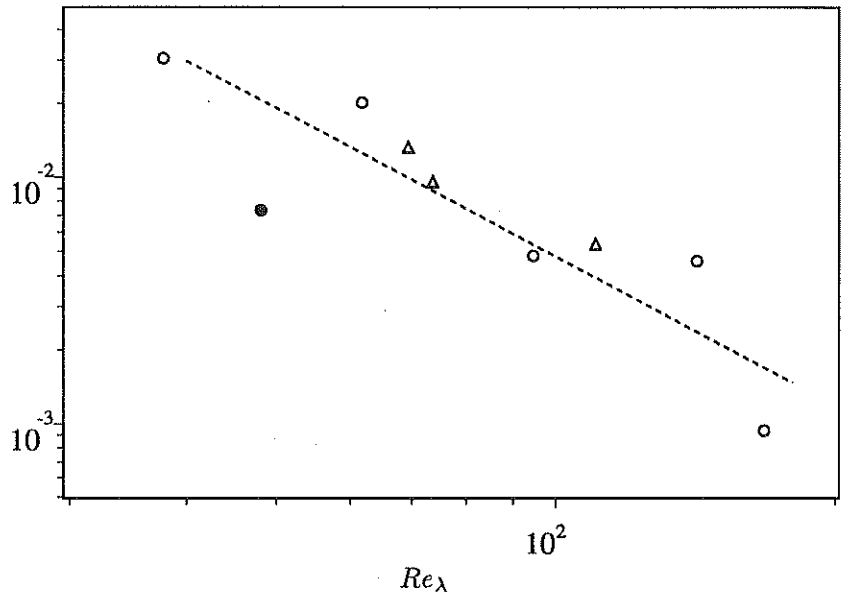

FIGURE 18. Volume fraction occupied by vorticity above the average detected in worms. ○ : viscous simulations, low wave number forcing; ● : viscous, middle wave number forcing; △ : hyperviscous; dashed line has slope -2.

elongation of the worms, $\ell_r/ < r >$, although large and increasing with Re_λ, never exceeds 10–20 in our range of Reynolds numbers.

A remaining problem is the growth of the circulation of the vortices with Re_λ. It was noted in JWSR that this implies an increase of the Reynolds number of the azymuthal motion of the individual structures and that at some point those structures should become unstable. We still feel that way, but we have no way of predicting the conditions for this instability.

We have also shown that the volume fraction occupied by worms decreases as Re_λ^{-2}. This is somewhat misleading and should be understood in relation to the decrease of their radii. If we remember that $\eta \sim Re_\lambda^{-3/2}$, it follows that the accumulated length of the structures grows like $L_\epsilon Re_\lambda$, and their total "number" per unit volume, as Re_λ. This is difficult to reconcile with their increasing instability as their Reynolds number increases. It has been proposed recently that an internal structural transition might exist in turbulence at $Re_\lambda \approx 10^3$, resulting in a decrease of intermittency (Tabeling *et al.* 1994). If this is confirmed, it could possibly resolve the present dilemma.

Finally, we have described the effect of hyperviscosity in isotropic simulations. The resulting spectra are dominated by large humps in the near dissipation region, which extend to the last wave number decade of the inertial range. They seem to be generated by the energy "bottleneck" produced by the inhibition of the energy cascade by viscosity.

Acknowledgments

The simulations were carried out on the Intel hypercube at NASA Ames Research Center and on the Intel Paragon at Wright Patterson AFB. The assistance of these computer centers' personnel is also gratefully acknowledged.

REFERENCES

BATCHELOR, G. K. 1953 *The theory of homogeneous turbulence.* Cambridge Univ. Press.

BORUE, V. & ORSZAG, S. A. 1994 Forced three-dimensional homogeneous turbulence with hyperviscosity. Preprint.

FALKOVICH, G. 1994 Bottleneck phenomenon in developed turbulence. *Phys. Fluids.* **6,** 1411-1414.

JIMÉNEZ, J. 1994a Hyperviscous vortices. *J. Fluid Mech.* **279,** 169-176.

JIMÉNEZ J. 1994b Resolution requirements in turbulence. *CTR Annual Res. Briefs*

JIMÉNEZ, J. & WRAY, A. A. 1994 Columnar vortices in isotropic turbulence. *Meccanica.* to appear.

JIMÉNEZ, J., WRAY, A. A., SAFFMAN, P. G. & ROGALLO, R. S. 1993 The structure of intense vorticity in isotropic turbulence. *J. Fluid Mech.* **255,** 65-90.

MESTAYER, P. 1982 Local isotropy and anisotropy in a high-Reynolds-number turbulent boundary layer. *J. Fluid Mech.* **125,** 475-503.

MESTAYER, P., CHOLLET, J. P. & LESIEUR, M. 1983 Inertial subrange of velocity and scalar variance spectra in high-Reynolds-number three-dimensional turbulence, in *Turbulence and chaotic phenomena in fluids* (T. Tatsumi, ed.), 285-.

ROGALLO, R. S. 1981 Numerical experiments in homogeneous turbulence. *NASA Tech. Mem..* **81315,** see also Canuto, C., Hussaini, M. Y., Quarteroni, A. and Zang, T. A.,*Spectral methods in fluid dynamics.* Springer (1981), pp. 85-86.

RYZHENKOVA, I. V. & FALKOVICH, G. E. 1990 Effect of dissipation on the structure of a stationary wave turbulence spectrum. *Sov. Phys. JETP.* **71,** 1085-1090.

SADDOUGHI, S. G. & VEERAVALLI, S. V. 1994 Local isotropy in turbulent boundary layers at high Reynolds number. *J. Fluid Mech.* **268,** 333-372.

SHE, Z-S. & JACKSON, E. 1993 On the universal form of the energy spectrum in fully developed turbulence. *Phys. Fluids A.* **5,** 1526-1528.

TABELING, P., ZOCCHI, G., BELIN, F., MAURER, J. & WILLAIME, H. 1994 Probability density functions, skewness and flatness in large Reynolds number turbulence. Preprint.

TOWNSEND, A. A. 1951 On the fine scale structure of turbulence. *Proc. Roy. Soc. London.* **A 208,** 534-542.

VAN ATTA, C. W. & ANTONIA, R. A. 1980 Reynolds number dependence of skewness and flatness factors of turbulent velocity derivatives. *Phys. Fluids.* **23,** 252-257.

VERZICCO, R., JIMÉNEZ, J. & ORLANDI, P. 1994 On steady columnar vortices under local compression. Preprint.

YAKHOT, V. & ZAKHAROV, V. 1993 Hidden conservation laws in hydrodynamics: energy and dissipation rate fluctuation spectra in strong turbulence. *Physica.* **D 64,** 379-394.